Fundamentals of Focused Ion Beam Nanostructural Processing: Below, At, and Above the Surface

Citation

MoberlyChan, Warren J., David P. Adams, Michael J. Aziz, Gerhard Hobler, and Thomas Schenkel. 2007. Fundamentals of focused ion beam nanostructural processing: Below, at, and above the Surface. MRS Bulletin 32(5): 424-432.

Published Version

http://www.mrs.org/s_mrs/sec_subscribe.asp?CID=8910&DID=195529&action=detail

Permanent link

http://nrs.harvard.edu/urn-3:HUL.InstRepos:2794940

Terms of Use

This article was downloaded from Harvard University's DASH repository, and is made available under the terms and conditions applicable to Other Posted Material, as set forth at http://nrs.harvard.edu/urn-3:HUL.InstRepos:dash.current.terms-of-use#LAA

Share Your Story

The Harvard community has made this article openly available.
Please share how this access benefits you. Submit a story.

Accessibility

Fundamentals of Focused Ion Beam Nanostructural Processing: Below, At, and Above the Surface

Warren J. MoberlyChan, David P. Adams,
Michael J. Aziz, Gerhard Hobler,
and Thomas Schenkel

Abstract

This article considers the fundamentals of what happens in a solid when it is impacted by a medium-energy gallium ion. The study of the ion/sample interaction at the nanometer scale is applicable to most focused ion beam (FIB)–based work even if the FIB/sample interaction is only a step in the process, for example, micromachining or microelectronics device processing. Whereas the objective in other articles in this issue is to use the FIB tool to characterize a material or to machine a device or transmission electron microscopy sample, the goal of the FIB in this article is to have the FIB/sample interaction itself become the product. To that end, the FIB/sample interaction is considered in three categories according to geometry: below, at, and above the surface. First, the FIB ions can penetrate the top atom layer(s) and interact below the surface. Ion implantation and ion damage on flat surfaces have been comprehensively examined; however, FIB applications require the further investigation of high doses in three-dimensional profiles. Second, the ions can interact at the surface, where a morphological instability can lead to ripples and surface self-organization, which can depend on boundary conditions for site-specific and compound FIB processing. Third, the FIB may interact above the surface (and/or produce secondary particles that interact above the surface). Such ion beam–assisted deposition, FIB–CVD (chemical vapor deposition), offers an elaborate complexity in three dimensions with an FIB using a gas injection system. At the nanometer scale, these three regimes—below, at, and above the surface—can require an interdependent understanding to be judiciously controlled by the FIB.

Introduction

The focused ion beam (FIB) is becoming an ideal tool for growing, sculpting, infusing, and observing small shapes in an ever-widening range of applications. In conjunction with scanning electron microscopy (SEM) as well as an increasing variety of add-on tools (micromanipulators, gas-injection systems, and spectroscopic and crystallographic analysis), the FIB can prototype devices, characterize structures *in situ*, and provide site-specific extractions for further *ex situ* processing or as sample preparation for other analyses.[1–3] Ion beam processing predates FIB, ranging from processing films for semiconductor devices to the preparation of transmission electron microscopy (TEM) samples,[4] and the ion/surface interaction has been understood and optimized in one-dimensional processing at doses up to roughly $10^{15}/cm^2$ (e.g., semiconductor doping). The FIB has extended the applications to a regime in which localized, three-dimensional (3D) ion/surface interactions are important, with doses of $\sim 10^{18}/cm^2$ and unprecedented current densities. The FIB as a processing or analysis tool has commonly used a fixed accelerating voltage and ion species (30 keV Ga); however, multispecies ion sources with variable voltage (<1 kV to >50 kV) are promising.[5] New FIB tool capabilities are being developed to meet more stringent requirements, such as TEM sample preparation with reduced surface damage and shallower implants driven by further miniaturizations of microelectronic devices. Traditionally, the ion/surface interaction caused a damage zone that often had to be subsequently removed by chemical etching or annealing processes. A damage zone of a few nanometers, whether implanted below or redeposited above the surface, often can be tolerated for microdevices but not for nanodevices. With 3D site specificity in an FIB, that which was termed "damage" or "artifact" may be controlled, understood, and even utilized for nanostructures.

As FIBs evolve from processing microdevices to nanodevices, some differences arise. FIB micromachining has become a broad field of its own,[6] and a future field of FIB nanomachining needs further development. Computer-controlled micromachining presupposes that the tool operates at a constant etch rate. For FIB machining at the nanometer scale, however, sputter yields may no longer be considered constants. The present-day FIB offers a range of currents and beam sizes, with a common smallest beam of 4–6 nm. Future FIB nanomachining may need a smaller spot; however, an energy reduction will be required to limit the present beam spread of 4–20 nm inside the sample (e.g., Figure 1). Furthermore, at the micron scale, the initial damage done by the FIB during setup of the process can be ignored, enabling quick FIB imaging and beam shifts (and/or computer image recognition) to be performed with impunity. However, at the nanometer scale, such FIB setup damage cannot be tolerated. This will require more reliable
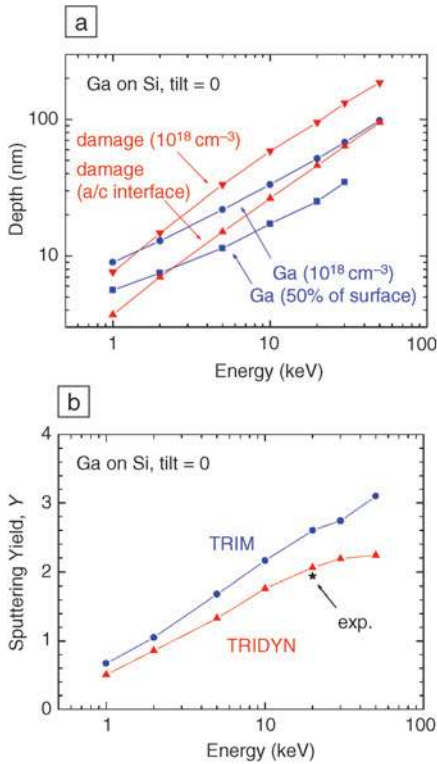
Figure 1. (a) Range of Ga and damage profiles in Si at different concentration levels. (b) Sputtering yields of Si bombarded with Ga as a function of energy as calculated by TRIM (neglecting the implanted Ga ions) and by TRIDYN (after a steady-state implantation profile has developed). The star corresponds to an experimental result.[12]

concentric dual-beam systems, with the SEM or other technologies (e.g., Figure 2) providing precise site-specific setup for FIB nanostructuring. Developing FIBs will overcome many present-day engineering hurdles, yet the physics of the ion/surface interaction will remain essentially the same. Although larger structures of the past have compelled individual study of interactions only below, at, or above surfaces, future small 3D structures will require a more comprehensive, interdependent understanding of all three.

FIBs *Below* the Surface: Local 3D Implantation and Single Dopants

When an energetic ion enters a surface, several effects occur, including implantation, damage, mixing, electron emission, and chemical reactions, in addition to sputtering. These physical phenomena are similar for FIBs or broad static beams (reviewed earlier);[4] however, lateral confinement differences arise when FIB per-

forms direct-write of nanometer-scale structures.

The minimum feature size is determined by beam width, ~4–10 nm in state-of-the-art FIBs. The spread of the collision cascade (Figure 1a) does not influence sputtering as long as the beam is normal to the surface. Monte Carlo simulations of these conditions (Figure 1b) show that most sputtered atoms originate from a 1 nm³ volume around the impact point.[7] In contrast, beam effects below the surface have a wider lateral spread. For example, the full width at half maximum (FWHM) of the lateral dopant distribution caused by a zero-width 30 keV Ga$^+$ beam in Si is 20 nm.

Ion effects below the surface are sometimes intended (e.g., doping) and sometimes unintended (e.g., samples made amorphous during FIB preparation). In both cases, it is desirable to estimate the range as the sum of the projected range, R_p, plus several standard deviations, σ_p, of the implant profile $R_p + n\sigma_p$, where n is an integer and R_p and σ_p are easily calculated by SRIM (a program for calculating the stopping range of ions in matter).[7] Monte Carlo TRIM (transport range of ions in matter) simulates more accurate estimates of the dopant and displaced atom (vacancy) distributions for a flat surface, $f(x)$, assuming unit dopant dose and neglecting sputtering and the incorporation of the beam atoms into the surface. The effect of surface movement can be accounted for, while neglecting the volume of the implanted atoms and atomic mixing.[8] This leads to an expression for the atomic density $N(x)$ of the implanted or displaced atoms valid for dilute concentrations, where x is a variable involving spatial dimensions, and x' indicates a moving version of that variable:

$$N(x) = \frac{N_0}{Y} \int_x^{x+d} f(x')dx'. \quad (1)$$

N_0 denotes the atomic density of the target, Y the sputtering yield (which may also be estimated by TRIM), and d the thickness of the sputtered layer. In the steady-state limit $d \to \infty$, Equation 1 has been used to estimate the depth at which the Ga or displaced atom concentration drops to 10^{18} cm^{-3} for a Si target bombarded with a Ga beam at normal incidence (Figure 1a). Also, Equation 1 may estimate the depth of the amorphous layer using a critical displaced atom density of 10^{22} cm^{-3} for the crystalline to amorphous transition in Si.[9] Although Equation 1 becomes invalid for high concentrations, it qualitatively shows that the doping density decreases with increasing sputtering

yield. Thus for glancing angles, such as in TEM lamella preparation, the sputtering yield is increased and doping can be minimized. In contrast, when the effective sputtering yield is decreased by redeposition, such as at the bottom of a trench, the doping and damage levels are increased.

A doping density approaching the target density can only be treated by dynamic Monte Carlo simulations, which
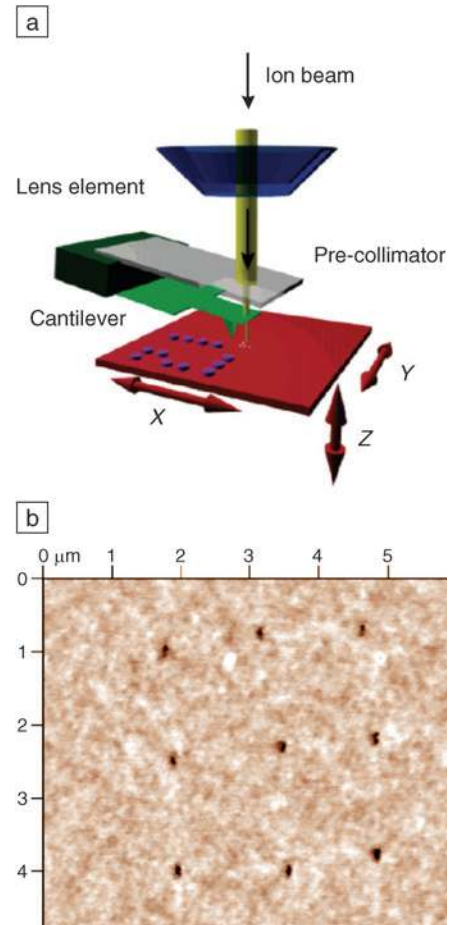

Figure 2. (a) Schematic illustration of a focused ion beam/scanning probe microscopy (FIB/SPM) tool enabling patterning without damage from tuning (from Reference 23). (b) *Ex situ* scanning probe image of a dot array formed in poly(methyl methacrylate) (30 nm thick) by ion implantation with scanning probe alignment (8 keV Ar^{2+}, 3×10^{13} ions/cm^{-2}). Dot size is 90 nm, about the same as the diameter of the hole in the scanning probe cantilever. Resolution-limiting effects such as beam divergence and the cantilever–sample distance, stage vibration, and resist resolution will become important for <20 nm features (courtesy of A. Persaud, Lawrence Berkeley National Laboratory).

consider the implanted ions as possible targets and takes their volume into account. The TRIDYN program (based on TRIM code)[10] calculates the position where the Ga density drops to 50% of its surface density for Ga implanted into Si (Figure 1a). For conventional FIB energies, the Ga doping is almost completely within the amorphous damage layer. However, at low energies, the highly doped Ga region extends beyond the amorphous depth. Thus, low-keV polishing of Si TEM lamellae[2,11] will still produce a thin Ga-rich layer as contamination even though negligible amorphous Si remains on the surfaces. Correct predictions of the surface densities are also essential to determine the correct sputtering yields because the beam and target atoms likely have different yields. Figure 1b shows a comparison of Si sputtering yields obtained by TRIM and TRIDYN, using default parameters in both cases. The TRIDYN results match recent experimental results.[12]

The dopant and damage ranges, as well as the sputtering yield, are changed under channeling conditions, where nuclear stopping is largely reduced. Channeling primarily occurs when the beam is aligned with a low-index crystallographic axis or plane and when the target is not made amorphous (such as pure metals). For most FIB ion species and energies and most targets, nuclear stopping dominates over electronic stopping. Thus, sputtering is reduced, and the ion range is considerably increased under channeling conditions.[4] Surprisingly, channeling may also play a role in targets becoming amorphous.[13] General-purpose simulation tools are now being developed to predict the exact 2D or 3D topography that forms under FIB irradiation.[14–16] Such tools are necessary in an iterative procedure to determine FIB parameters to obtain a desired nanosculpture.[12]

An ultimate goal of FIB is to process single dopant atoms using lower beam currents, faster computer control, and future design alternatives for alignment (tuning) and *in situ* metrology. Single defects and single dopant atoms can significantly alter the performance of electronic devices such as field-effect transistors, even at room temperature, for devices 10 nm in size. The corresponding variability of device performance because of discrete dopant distributions is a potential scaling barrier.[17,18] Single defects (even ones induced by cosmic radiation) can also significantly alter the performance of devices or lead to single-event upsets in memory cells, and understanding the effect of single-ion impacts on devices is important to improve radiation hardness. A comple-

mentary view considers classes of devices where functionality is based on the presence and precise manipulation of single dopant atom states. Coherent manipulation of spin states of phosphorus or antimony atoms in a silicon matrix has been envisioned as a path to scalable quantum computing.[19–21]

FIB doping of nanometer-scale devices was explored with tools available in the 1980s.[1,22] Besides throughput, several limitations persist for conventional FIB tools as precision ion implanters. Dopant species and implant energies are not easily varied in one tool, dose control is difficult, and most systems are not equipped with a mass analyzer. The development of high-brightness sources capable of producing ions of different species can ease the first restriction.[5] Achieving small spot sizes with variable beam energies has been difficult with traditional focusing columns. Finally, the ion beam must not image the region of interest during tune-up alignment, as this introduces an unwanted dopant dose. The latter requirement necessitates superb alignment of the ion beam with an electron beam (e.g., in dual-beam systems) and/or a high-precision stage for displacement of the sample from the tuning area into the region of interest.

The ideal precision implanter may eventually be able to deliver defined numbers of ions from elements with a range of kinetic energies from across the periodic table into precise locations in a device. Fabrication of a Kane-type quantum computer calls for placement of individual Group-V dopants into Si with a spacing of 20–30 nm and accuracy of a few nanometers. Radiation-induced single defects can alter transistor performance in sub-100-nm gate length devices, and testing these radiation effects requires reliable placement of ions into device channels. Factors contributing to placement accuracy are the effective beam spot size, range straggling caused by statistical energy loss processes, and diffusion during post-implant activation annealing. The last is sensitive to defect injection from the dielectric–silicon interface for specific dopants, which leads to enhancement of diffusion for phosphorus and retardation of diffusion for antimony in the presence of an imperfect SiO_2/Si interface. The highest placement accuracy is achieved with low-energy heavy ions. For 30 keV Ga+ beams, placement of single ions can be expected within the achievable beam spot sizes of about 10 nm. However, a low-intensity beam (~1 pA) provides a weak secondary electron image and still can induce damage during tuning/alignment.

An alternative to beam tuning in a nearby sacrificial region is to perform the imaging function with a scanning probe (Figure 2a). Here, the ion beam is collimated and transported through a small aperture; however, the sample is noninvasively imaged by a scanning force microscope (SFM) while the ion beam is off. This recently developed tool uses a piezoresistive force readout for SFM.[23] Holes are drilled into a silicon cantilever using a standard FIB and thin-film deposition. Holes with diameters as small as 5 nm are formed by drilling a large hole first and then reducing the hole diameter by deposition of a thin Pt film.[24] The collimator will deteriorate after extended beam exposure, but the dose for this can be estimated from the drilling conditions under which the aperture was formed in the first place. Also, perforated cantilevers can be refurbished after extended use (holes can be reshaped and imaging tips can be sharpened). Whereas a 5–10 nm imaging resolution is superb for FIB imaging, this modest resolution can be achieved in an SFM without excessive vibration isolation. With collimators of 5–10 nm in diameter, the integration of FIBs with SFMs offers a reliable route to precision doping of nanodevices.

Figure 2b depicts a pattern formed in resist by ion implantation with scanning probe alignment. To control processing, the detection of single-ion impacts can be monitored via detection of secondary electrons through the pick-up of the charge pulse of electron–hole pairs that form when ions impinge on semiconductors. The former is very universal, but requires a secondary electron yield of >1 for reliable single-ion detection. Secondary electron yields are material-specific but can be enhanced by lowering the work functions (e.g., depositing a low coverage of cesium). The kinetic energy and the charge state of the incident ions also affect SE yields.[25,26] The detection of ion beam–induced charge (IBIC) can be administered relatively noninvasively by electrical connections to samples tens of microns away from the region of interest.[27] The ultimate limit in single-ion placement depends on the ion energy and species, the target material, and the aperture size in the collimator. Optimized collimators can provide an ultimate placement resolution of <5 nm for low-energy heavy ions.

FIBs *At* the Surface: Morphology Evolution during Erosion

A starting surface is traditionally 2D flat, and yet FIB produces 3D structures with variable slopes and nanometer

tolerances that require improved understanding of 3D physics.

Three FIB issues can affect surface topography: machining, lithographic patterning, and the ion/surface interaction. First, as an engineering cutting tool, micromachining is becoming nanomachining, with correspondingly tighter tolerances. Second, the superior resolution of an FIB compared with photolithography invites its use for specialty direct-write patterning with ever-higher aspect ratios. Third, the ion–surface interaction physics depends on local slope and curvature; hence, the evolving 3D morphology at the nanometer scale is not fully predictable. At the micron scale, the machining or patterning capabilities of an FIB may be independently engineered.[6] Above the millimeter scale, the physics of broad-beam processing is a stand-alone science.[4] However, all three issues are colliding as FIBs process nanometer-scale shapes. This section compares the role of ion–surface physics on developing topography by FIB versus broad beam as well as the interactions among all three issues when fabricating nanostructures.

FIB tools are designed to expediently ion etch or machine surfaces, but such sputter etching typically roughens surfaces at submicron length scales. An ideal FIB might machine away one atom layer with neither disruption of the atoms in the next layer nor any residual disruptions above the surface. However, fast FIB etching requires high-energy ions that simultaneously interact with multiple layers. Energetic ions cause sputter etching (yield), surface diffusion, and local rearrangements of atoms in a disrupted surface zone. A morphological instability can self-organize with characteristic nanometer length scales and a wavelength of surface roughness that can be many times smaller than a broad static beam or many times larger than a 4–10 nm focused scanning beam. Conversely, when roughness is undesirable, it may sometimes be mitigated with beam rastering, sample rotation, or a combination thereof. FIBs may also produce very smooth surfaces for improved Auger depth profiling and TEM sample preparation.[1,2]

Experimentally, surface topographies spontaneously develop when targets are eroded by either broad static ion beams or a uniformly rastered FIB.[28–40] Although roughness is a bane during erosion of sputter targets used in physical vapor deposition, nanometer-scale structures such as ripples (Figure 3a), steps (Figure 3b and 3c), and dots (Figure 3d) inspire efforts to understand and manipulate surface instabilities. Judicious FIB control has
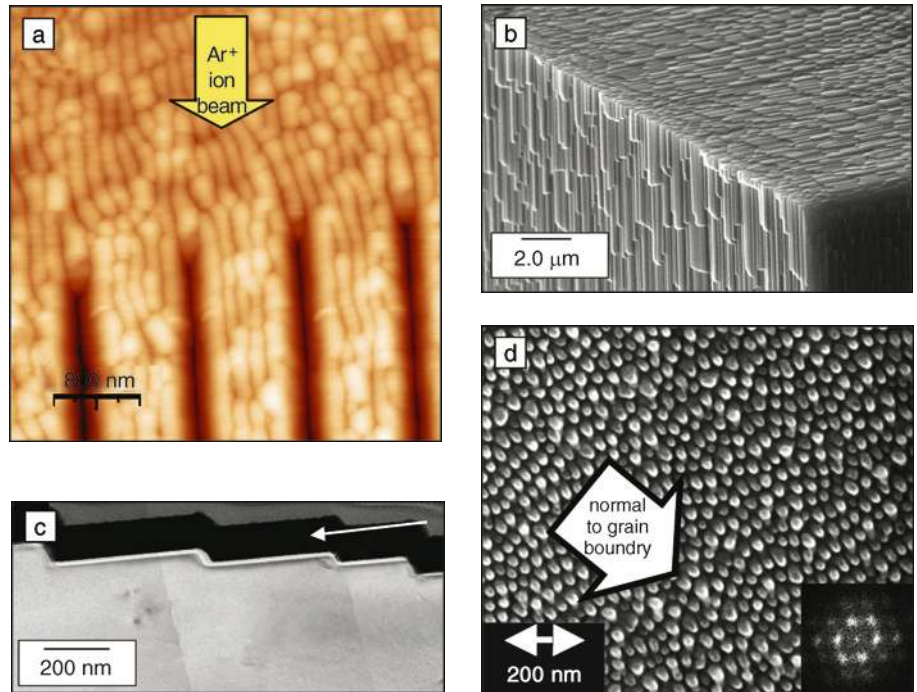

Figure 3. (a) Trenches milled with a Ga-FIB guide self-organized rippling on Si(001) at 540°C under subsequent broad 800 eV Ar+ beam at 45° from normal, projected beam vertical in image as shown (see Reference 52). (b) Scanning electron microscopy (SEM) image of diamond, showing three intersecting surfaces after FIB sputtering. Each surface was sputtered in equivalent near-grazing incidence geometry. (c) Cross-sectional transmission electron microscopy image of steps formed in diamond after FIB exposure at a high angle of incidence indicated by white arrow (from Reference 53). (d) SEM image of beryllium surface after Ga-FIB dose of ~8 × 10^18 ions/cm² at ±3° from normal. (Morphology changes in neighboring grain; see Reference 63.)

the potential to fabricate functional arrays of quantum dots.[41]

Theoretically, if $h(\mathbf{x})$ represents the surface topography when the ions approach the surface in the $-z$ direction, the local height change at $\mathbf{x} = (x,y)$ when an ion strikes the surface at $\mathbf{x}'$ is $\Delta h(\mathbf{x};\mathbf{x}')$. During sputter erosion with an instantaneous ion flux $J(\mathbf{x}')$, the surface morphology evolution is described by[42]

$$\frac{\partial h(\mathbf{x}, t)}{\partial t} = \iint J(\mathbf{x}') \, \Delta h\left(\mathbf{x}; \mathbf{x}'\right) d^2\mathbf{x}'. \qquad (2)$$

The complicating aspect of this integral equation is that $\Delta h(\mathbf{x};\mathbf{x}')$ depends on the local surface slope and curvature, but may also depend on higher-order derivatives. Hence, many theoretical approaches start with an approximation for this "kernel," $\Delta h(\mathbf{x};\mathbf{x}')$. Sigmund first identified an instability by assuming the kernel to be proportional to the nuclear energy deposition density at $\mathbf{x}$ in a collision cascade arising from an impact at $\mathbf{x}'$ and approximating the cascade shape with Gaussian ellipsoids beneath the surface.[28] Because concave regions of the surface are nearer their neighboring cascades than are convex regions, the predicted sputter yield is higher in the concave regions, leading to a morphological instability. By combining the kinetics of surface diffusion with an expansion of the Sigmund kernel in Equation 2, Bradley and Harper[31] provided a linear stability theory that predicted ripples with a characteristic spatial scale. Supplements to the theory are higher-order expansions, surface diffusion,[31,35,43] viscous flow,[32] shadowing,[33] crystallographic channeling effects,[44,45] redeposition,[46] and wave mechanics.[47,48]

Surface modulations are an intrinsic aspect of the ion erosion process, whether created by uniform FIB rastering or by a broad static beam.[36,49] Ripple orientation, wavelength, and amplitude depend on energy, dose, dose rate, inclination angle, temperature, and crystallography, as well as the ion and surface species. All of these parameters are similarly controlled for FIB[2] or broad-beam processing; however,

FIB enables higher current densities and 3D forms. FIB dwell time, spot size, overlap, scan pattern, and orientation provide a flexible group of parameters that can be controlled to produce intrinsic modulations; however, stepping outside limits (e.g., large negative overlap) can induce artificial ripples[50] that may be more aptly designated as patterning. The FIB's fast computer control of precise patterns and parameters can produce nanometer-scale, site-specific modulations and opportunities for rapid prototyping of developing surface morphologies,[39,49,51] especially with real-time imaging and *in situ* (dual-beam) metrology.[36,37,39,50]

Often a compound process including FIB will generate geometries that necessitate understanding boundary conditions. For example, prepatterned trenches (Figure 3a) influence the subsequent ripple development.[52] This structure could be made with photolithography followed by broad-beam processing, or trenches could be direct-written with an FIB to seed specific instabilities in successive FIB processes. Aziz and co-workers have observed several effects near boundaries, such as ripple reflection and interference[49] and ripple alignment with the sides of an FIB pit.[39] Wavelength can increase near walls.[50] Steeply sloped walls may propagate under uniform irradiation as shock fronts (Figure 4).[47] A range of high and low slopes all spontaneously evolve to the same final value. Whereas normal processing conditions may "smear out" initial features such as sharp edges, shock mechanics may provide a new level of nanoscale processing control, in which a dispersion of initial shapes all converge to identical final shapes under uniform irradiation.[47]

FIB ripples have been fashioned on crystalline[36,37,39,45,49,53,54] and amorphous[32,36] materials and even on frozen biological samples.[55] Ripples can be expected on amorphous surfaces based on the Bradley–Harper (B–H) theory,[31] and similarly the FIB can rapidly make crystalline surfaces become amorphous and then ripple. Even with an amorphous surface, some ripples may exhibit an orientation dependence on subsurface sample crystallography.[56] Modulations tend to facet on crystalline surfaces that do not become amorphous, but no theory corresponding to B–H covers instabilities on faceting surfaces. Single-crystal silicon provides an ideal surface for the study of various process controls on surface topographies,[33,35,49,57] as well as being of practical importance to facilitate such topographical control into device applications built on silicon technology.
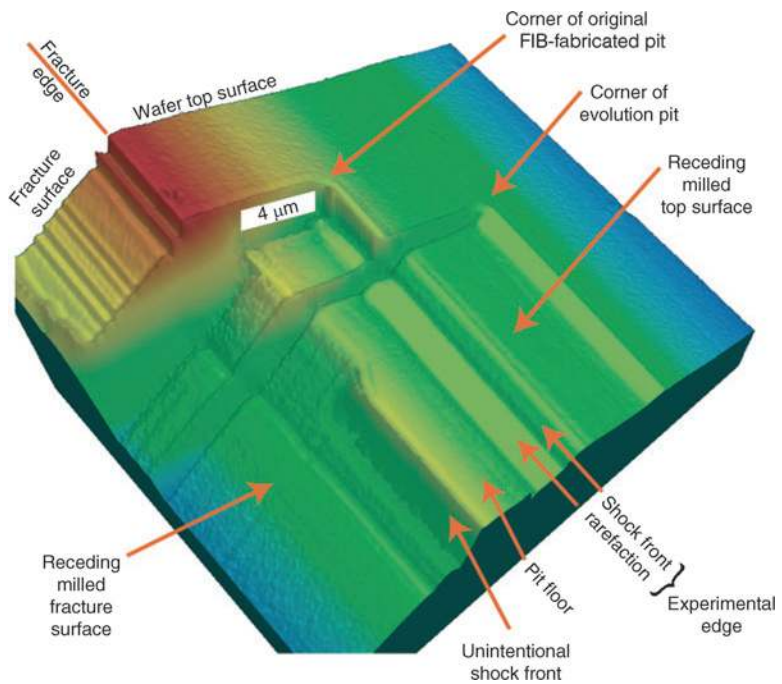

Figure 4. Controlled by shock mechanics, uniform FIB irradiation can cause features to sharpen up rather than to dissipate as expected. Edge of FIB-fabricated pit propagates laterally under uniformly rastered FIB irradiation ("evolution pit"), while the slope evolves downward to a dynamically selected value ("shock front"). A portion of the slope is evolving upward toward the same dynamically selected value ("unintentional shock front"). (From Reference 47.)

Diamonds also provide beautiful ripples,[36,40,50,53,58,59] with the optimization of FIB processing of micromachining toolbits[53] providing an ideal study of the interaction of angle, yields, chemistry, and ripples. By increasing the angle of ion incidence, Adams[53] and Datta[36] observe three classic regimes: smooth, 1D ripples, and steps (Figure 3b). In fact, the smooth regime can produce surfaces smoother than the original.[50,53] Because a smooth amorphous surface contradicts B–H theory, some improvements to the Sigmund kernel are needed.[42] A smooth surface finish is typically requested of micromachining, and chemically enhanced FIB is commonly applied to reduce surface roughness.[53,60] However, more recent work uses the same chemistry to enhance ripple growth.[50]

Since yield depends on local slope,[28] the etch rate changes as ripples take shape. It is not always possible to achieve a steady-state etch rate with constant ripple wavelength and amplitude, and no present theory can reliably predict morphology evolution. Ripple wavelength can increase with dose[57] or be constant,[35] and ripples can be traveling waves,[37] with enhanced mobility facilitated by line defects. Most often amplitudes saturate at a small frac-

tion of wavelength.[33,43,40,57] However, modulations with high aspect ratio[39,49,50] offer intriguing possibilities, such as for high-surface-area catalysts. Many models and experiments indicate the wavelength saturates as a function of fluence, which is of practical utility to reliable future FIB processes.[33,36,43,57] Sigmund's theory[28] has yield increasing as ripples grow, but Carter[61] models a subsequent decrease in yield as wavelength increases. The yield/ripple dependence is further complicated for compound materials that exhibit a compositional transient period before stabilizing yield.[62] Escalating redeposition in a deepening FIB pit can cause ripple wavelength to increase with aspect ratio while the yield decreases.[50] Although chemical enhancement of sputter yield is typically designed to provide smoother surfaces in semiconductor processing, the chemical vapor may also aid ripple growth.[50] FIB issues that cause ripples to grow too large bode poorly for their use as nanostructures; however, recent FIB processing of a diamond-like film has also produced subnanometer ripples.[63] Even at the micron scale, understanding the influence of aspect ratio on yield is critical for precision machining[64] and TEM sample preparation.[65] Because ripples change

yield and yield changes ripples, the etch rate may not be treated as constant in FIB processing of 3D nanostructures.

Redeposition (or recondensation) is often hard to avoid during FIB processing[50,51,66,67] and may play a role in ripple formation.[31,68] Special sample geometries and versatile FIB angles of incidence can limit redeposition[47] and are especially critical for micromachining applications[64] and TEM sample preparation.[65] Because redeposition refers to all cases of atoms returning to surfaces and may include the interplay of multiple neighboring surfaces, ripples at the bottom of an FIB pit[39] are modified by redeposition and dropping yields.[61] Because redeposition can be measurable in a micron-size FIB pit even at low aspect ratios,[50] it may similarly affect nanometer-scale ripple formation regardless of the beam size[46,63] (e.g., using modeling parameters in the computer program Kalypso[69]). Modeling of redeposition—and its avoidance—is a major concern in TEM preparation.[66] Trajectory models[69] show that atoms leaving a surface with low kinetic energy may return, depending on surface geometry and the relative charge state between atom and surface, with the latter being influenced by the incident ions and exiting secondary electrons. Erosion ripples can also be a consequence of laser machining and associated redeposition;[70–73] however, FIB offers more precise and reliable control of these nanometer-scale topographies.

The modern FIB commonly operates with 30 keV Ga ions, resulting in many surfaces that are amorphous. The top atom layers contain more than 10% gallium after FIB.[64,74,75] These artifacts may place practical limits on the use of these modified surfaces. It may be possible to restore crystallinity by continued ion bombardment,[76] as well as by thermal annealing. A chemical etch may remove gallium but may also disrupt the FIB-processed shapes, especially when gallium composition is also modulated. Residual gallium may limit the utility of self-organizing 2D dot arrays processed by FIB,[49,63] as well as those integrated with direct-write FIB lithography.[41,77,78] However, ripples of undesirable chemistry and ripples at the bottom of an FIB pit may become useful after imprint patterning transfers such modulated topographies to the top of nanometer-scale pedestals. The present development of multisource FIBs using inert ions will facilitate more chemically compatible surface structures.

FIBs *Above* the Surface: FIB–CVD

FIB-assisted chemical vapor deposition (FIB–CVD)[79–85] provides an approach to produce nanostructures *above* a surface. FIB–CVD is essentially a thin-film growth technique that can be used for site-specific deposition of various materials. Modern FIB systems are capable of depositing metals, oxides, and carbon with spatial resolution that is often better than electron beam lithography. Encompassing self-organization processes and predeposited molecular catalysts, FIB–CVD may also produce yet smaller structures within a single local pattern.

FIB–CVD involves directing a focused ion beam onto a surface that has adsorbed a precursor gas (e.g., an organometallic) having an element or compound intended for deposition as a constituent. The FIB strikes the surface layer and activates the break-up of the molecular species, thereby leading to deposition. Typically, the gaseous precursor species are delivered to a surface by a nearby capillary tube, a nozzle, or sample box having an opening for beam entry. This establishes a local pressure between 0.1 and 10 mTorr,[86,87] yet retains ~10^{-6} Torr in the remaining vacuum chamber. The precursor must be volatile for delivery to the surface, yet it must adsorb in sufficient quantity[88] to create a deposit upon beam stimulation.

Various processes influence FIB–CVD, including the effects of gas delivery, site-specific adsorption/desorption, surface migration, dissociation, incorporation of impurities, implantation, sputtering, and the beam scan parameters (including ion current density).[1,89–92] Specialty nozzles assist growth of and onto complex 3D geometries.[93] In general, molecular dissociation occurs upon ion bombardment, and a deposit can grow in thickness provided that sputtering or other competing removal processes do not occur at larger rates. Examples of precursor gases include tungsten hexacarbonyl [$W(CO)_6$], trimethyl aluminum [$Al(CH_3)_3$], tetraethoxysilane (TEOS), and Cu(I) hexafluoroacetylacetonate vinyltrimethylsilane.

Many earlier studies have created several key applications for FIB and are the foundations for today's prototyping[6,94,95] and advanced materials analyses.[44,96] FIB–CVD is commercially successful for semiconductor device restructuring and lithographic mask repair.[97,98] For example, opaque carbon is produced when Ga-FIB energizes adsorbed organic monomers.[82,88,99,100] This provides a method for correcting clear photomask defects in a one-step process.

More recently, FIB–CVD was used for fabricating nanometer-scale sensors[101,102] and devices,[103] making electrical contacts to nanostructures,[104] and joining for lift-out specimens for TEM.[2,30] This deposition technique offers flexible access to complex geometries that enable growth of nanometer-scale solid free-form or bridging structures via computer-aided drafting/computer-aided manufacturing (CAD/CAM) modules.[105,106] Figure 5a highlights FIB–CVD capabilities for microbiological experiments.[107] A diamond-like carbon tool is grown onto the end of a glass capillary by directing a 30 keV Ga ion beam onto the surface while exposing the surrounding volume with phenanthrene ($C_{14}H_{10}$). Penetration of an *Egeria densa* leaf cell well was demonstrated, as shown in Figures 5b–5e. Additional FIB–CVD-fabricated instruments were used to extract and collect organelles contained within the cell.[107]

The FIB–CVD ability to deposit material in targeted regions with submicron precision has also benefited the materials analysis community by enabling reliable site-specific TEM sample preparation. This technique (and electron beam CVD) can "grow" a protective, conductive, capping layer before FIB cross-sectioning, thereby preventing unwanted artifacts in a thinned specimen. FIB–CVD is also instrumental for transferring small specimens, such as welding for TEM lift-out samples.[2]

In an attempt to aid prototyping and device structuring, recent studies of FIB–CVD evaluated and improved the properties of deposits.[108–110] Metals deposited by FIB–CVD are sufficiently conductive for most applications. Recent details of the transport properties of FIB–CVD-Pt nanointerconnects show high disorder,[108] probably because of the presence of impurities. FIB–CVD-Pt has a small residual resistivity ratio and a Debye temperature that differs substantially from that of pure Pt. Lower electrical resistivity of deposited metals was achieved by changing the reaction process.[111] For example, deposited Au can be improved by a subsequent anneal to drive off impurities.[110] Heating the target via a remote laser led to Cu lines with a resistivity of 3 μΩ cm (compared with 150–200 μΩ cm when no laser radiation is used).[87] Lower resistivity correlates to reduced incorporation of decomposition products. FIB–CVD studies have improved electrical and optical properties for deposited dielectrics,[109,112] where the addition of oxygen (or water) during deposition can significantly decrease the carbon content in SiO_2.[112] Additionally, experiments with different precursors successfully increased the resistivity (~8×10^{11} Ω cm) and breakdown field (~650 V/μm) of SiO_2[113] by controlling deposition yields (i.e., deposited SiO_2 units per incident ion) to reduce Ga in the SiO_2.[113] Despite these

improvements, there is little known regarding conduction and the role of defects in insulators made by FIB–CVD. Finally, the mechanical properties of materials made by FIB–CVD were evaluated[114–116] for potential structural applications such as those involving cell cutting and nanomanipulation. Recent studies have quantified the Young's modulus (~100 GPa), shear modulus (~70 GPa), and spring constants (0.47–0.07 N/m) of diamond-like carbon grown by FIB–CVD.[116]
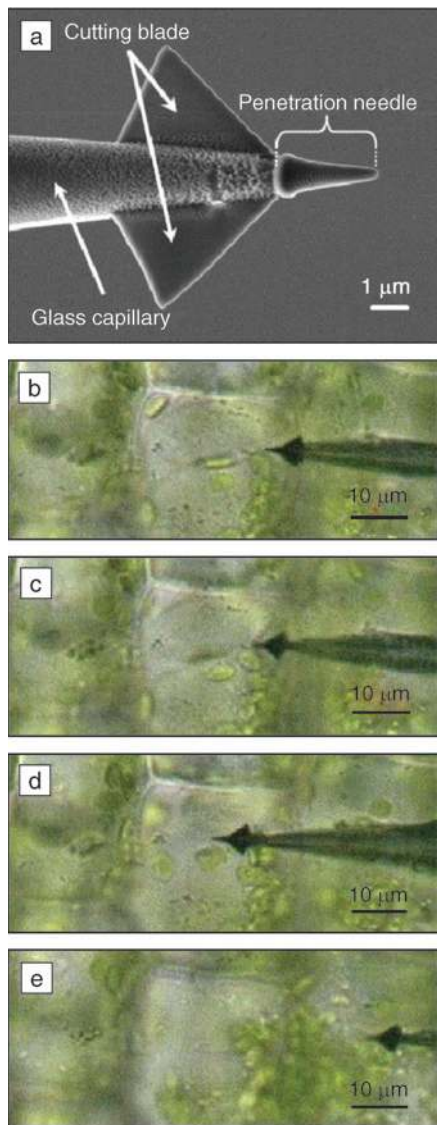
Figure 5. (a) SEM image of a cell wall cutting tool fabricated by FIB–CVD. The series of optical microscope images show (b) the cutting tool approaching a cell wall, (c) cell wall pushed by the needle of the tool, (d) cell wall cut by a diamond-like carbon blade of the tool, and (e) tool removed from cell. (Results by permission from R. Kometani.[107])

Ga is incorporated into deposits made by FIB–CVD with estimates of Ga concentration as high as 28 mol%[117] that may limit the usefulness of some structures. Future FIB development will offer less invasive ion species.[118] Nevertheless, the site-specificity of Ga-FIB–CVD outweighs the contamination effects for many applications.[1,2,92,97,98,119]

The modern FIB often comes packaged as a dual-beam FIB–SEM, which has expanded the development of electron beam–assisted deposition (EBAD). EBAD (SEM–CVD) generally provides slower growth rates, produces less dense structures, and may contain more lingering impurities from the processing gas. A comparison of SiO_2 grown with the FIB and the SEM determined both to have useful dielectric properties.[109] Although the FIB–SEM tool has engineered an electron beam and an ion beam to impinge the same site-specific surface for a decade, only recent advances have enabled both FIB and SEM to be "on" simultaneously. The fields of both charged particle beams disrupt each other; however, quicker computer controls enable interlaced scanning of the two beams[120] and new lens design can mitigate the interference.[121] Either the FIB or SEM can enable direct-write deposition (ion beam or electron beam–assisted deposition),[109] but now the opportunity exists to use the FIB and SEM to cut and paste, respectively, in (nearly) the same place at the same time. Figure 6 models the case where a solid source material was introduced on the end of a micromanipulator. The FIB and SEM beams were deliberately misaligned[63] so that the FIB was nanosputtering the source material while

the SEM was causing site-specific electron beam–assisted growth on a nearby substrate. The addition of gases via a gas-injection system may enhance growth or enable compound material growth. Also, it becomes possible to protect these nanostructures by encapsulating them *in situ* with an FIB–CVD overcoat, such as a silica layer from a TEOS gas-injection system needle. When a source material is prohibitively expensive and/or hazardous, the consumption of only zeptoliters of material via this multibeam process offers new opportunities, as compared with traditional lithographic processing.

Future FIBs

Future FIBs will help shape nanostructures, whether they are implanted beneath or grown above the surface. Yet, the FIB will remain primarily an ion etching or micromachining process providing reproducible etch rates (yield) for a given material system. FIB micromachining has proven reliable because of the tool's trustworthy constant etch rate; however, FIB sculpting at the nanometer scale requires more careful understanding of sputter yields that are no longer constants. The high current densities of digitally controlled FIBs instantly form holes; thus, all FIB processing involves sputtering of local angles and aspect ratios. Recent works have monitored change to sputtering yield due to local angle and chemistry additions,[53] but also noted a change in yield as a function of dose (Figure 7a)[59] and aspect ratio (Figure 7b).[50] Attempts to control and understand these changes justify further study of the nature of the ion–surface interaction in these tools
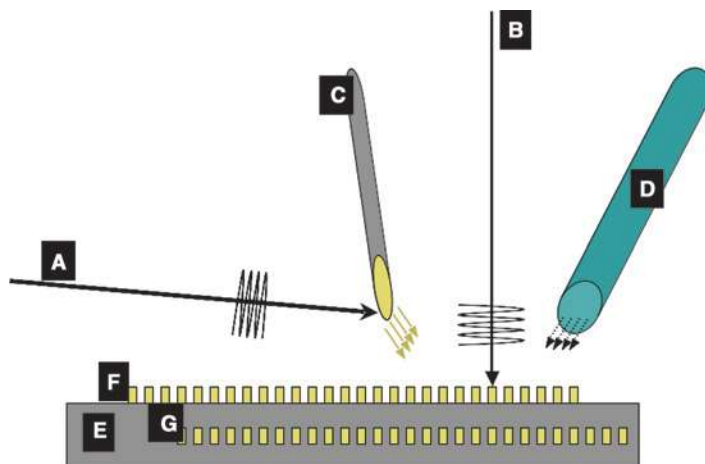
Figure 6. Simultaneous dual-beam processing enables the FIB (A) to cut while an SEM (B) deposits nearby. This can direct-write nanometer-scale structures (F) on a substrate (E), consume only a zeptoliter (10⁻²¹ liter) source that arrives attached to a micromanipulator (C) and potentially form compounds or protective overcoats (G) via a gas-injection system (D).

where the ion beam is focused to the nanometer scale.

The future FIB will be a faster processing tool, because of computers and vendor developments, and the future smaller volume of nanostructures will make the FIB's cut-and-paste skills seem even faster. The direct-write capabilities of the FIB (cut, paste, or implant) offer great resolution (at or above or below the surface, respectively), but the ~100 ns dwell time of the state-of-the-art FIB remains too slow for direct competition in device fabrication. Nanostructures 10 nm in diameter grown serially across a single 12-in. wafer would require more than two years, not including the time to get the FIB from one nanostructure to the next. For specialty processes and site-specificity, however, the FIB is quite fast. For example, FIB-multibeam deposition and FIB-micromanipulated transplants (Figure 6) of one radioactive energy source inside each microelectronic processor (~1000 per wafer) would consume affordable time

while utilizing a quantity of hazardous material below levels of environmental concern. Traditional top-down lithographic processing has a large percentage of waste, which will become greater for processing nanostructures. Ninety percent of the sputtered target is not incorporated into thin-film growth, and another 90% of the thin film itself becomes waste during patterning. (Additional hazardous wastes arise from cleaning and photolithography processes.) The various direct-write capabilities in the FIB involve much smaller (zeptoliter-scale) sources and less waste, thereby making more material selections viable. Furthermore, the FIB provides a containment vessel, protecting both people and product, and lessening cleanroom requirements that will be harder to achieve for nanostructuring.

FIBs and dual-beam FIB–SEMs provide stand-alone metrology, and especially on-the-fly metrology during *in situ* processing. However, microtechnology applications accept the initial damage during

FIB setup. Even FIB–CVD ignores the surface damage caused by 30 keV ions before any growth can occur. (Granted, when the FIB etches away a native oxide, it actually enables the subsequent Pt metallization growth with better conduction.) Fortunately, some setup damage can be mitigated by new processes, which are designed inside the FIB such as cryolithography. Small structures such as nanotubes are consumed when FIB patterning is attempted. However, applying a temporary protective coating inside the FIB enables damage-free processing. Future nanostructuring will require elimination of all setup damage. More control of the site-specificity of the FIB will be consigned to the concentricity of the SEM and/or other add-on technologies, such as the SPM. Most important, a continuous improvement in the understanding of the ion/sample interactions below, at, and above the surface will further advance FIB processing of nanostructures.
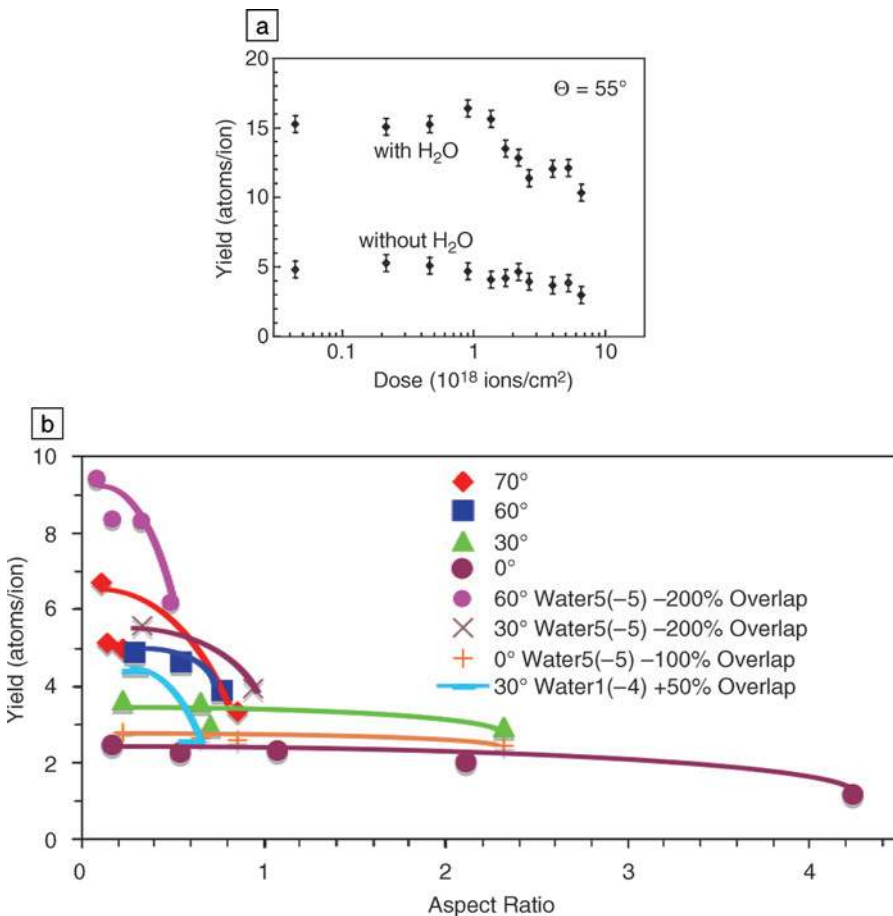
Figure 7. FIB processing of complex geometries of nanometer-scale structures will not experience a constant etch rate. Yield can decay as (a) a function of dose (from Reference 59) and/or (b) a function of aspect ratio (from Reference 50).

References

1. J. Orloff, M. Utlaut, L. Swanson, *High Resolution FIB and its Applications* (Kluwer Academic/Plenum, New York, 2003).
2. L.A. Giannuzzi, F.A. Stevie, *Introduction to FIB* (Springer, New York, 2005).
3. See the introductory article by C.A. Volkert and A.M. Minor in this issue.
4. E. Chason et al., *Appl. Phys. Rev.* **81** (10), 6513 (1997).
5. Q. Ji et al., *Nucl. Instrum. Methods Phys. Res. Sect. B* **241**, 335 (2005).
6. See the article by R. Langford et al. in this issue.
7. J.F. Ziegler, SRIM (2006), http://www.srim.org.
8. H. Ryssel, I. Ruge, *Ion Implantation* (Wiley, New York, 1986).
9. H. Cerva, G. Hobler, *J. Electrochem. Soc.* **139** (12), 3631 (1992).
10. W. Möller, M. Posselt, *TRIDYN_FZR User Manual* (Forschungszentrum Rossendorf, Dresden, Germany).

11. L.A. Giannuzzi, *Microsc. Microanal.* **12** (2), 1260 (2006).

12. D.P. Adams, M.J. Vasile, *J. Vac. Sci. Technol., B* **24** (2), 836 (2006).

13. A. Lugstein, W. Brezna, G. Hobler, E. Bertagnolli, *J. Vac. Sci. Technol., A* **21**, 1644 (2003).

14. G. Hobler, A. Lugstein, W. Brezna, E. Bertagnolli, in *Mater. Res. Soc. Symp. Proc.* **792**, L.-M. Wang et al., Eds. (Warrendale, PA, 2003) pp. 635–640.

15. H.B. Kim, G. Hobler, A. Lugstein, E. Bertagnolli, *J. Micromech. Microeng.* (2007) in press.

16. W. Boxleitner, G. Hobler, *Nucl. Instrum. Methods Phys. Res., Sect. B* **180**, 125 (2001).

17. T. Shinada, S. Okamoto, T. Kobayashi, I. Ohdomari, *Nature* **437**, 1128 (2005).

18. T. Schenkel, *Nature Mater.* **4**, 799 (2005).

19. B.E. Kane, *Nature* **393**, 133 (1998).

20. T. Schenkel et al., *Appl. Phys. Lett.* **88**, 112101 (2006).

21. R.G. Clark et al., *Philos. Trans. R. Soc. London, Ser. A*, **361**, 1451 (2003).

22. R.H. Reuss et al., *J. Vac. Sci. Technol., B* **4**, 290 (1986).

23. A. Persaud et al., *Nano Lett.* **5**, 1087 (2005).

24. T. Schenkel et al., *J. Vac. Sci. Technol., B* **21**, 2720 (2003).

25. R.A. Baragiola, *Nucl. Instrum. Methods Phys. Res. B* **78**, 223 (1993).

26. T. Schenkel et al., *Microelectron. Eng.* **8**, 1814 (2006).

27. D.N. Jamieson et al., *Appl. Phys. Lett.* **86**, 202101 (2005).

28. P. Sigmund, *J. Mater. Sci.* **8**, 1545 (1973).

29. B.R. Appleton et al., *Appl. Phys. Lett.* **41** (8), 711 (1982).

30. F.A. Stevie, P.M. Kahora, D.S. Simons, P. Chi, *J. Vac. Sci. Technol., A* **6**, 76 (1988).

31. R.M. Bradley, J.M.E. Harper, *J. Vac. Sci. Technol., A* **6**, 2390 (1988).

32. T.M. Mayer, E. Chason, A.J. Howard, *J. Appl. Phys.* **76** (3), 1634 (1994).

33. G. Carter, V. Vishnyakov, *Phys. Rev. B* **54**, 17647 (1996).

34. S. Facsko et al., *Science* **285**, 1551 (1999).

35. J. Erlebacher et al., *Phys. Rev. Lett.* **82** (11), 2330 (1999).

36. A. Datta, Y.R. Wu, Y.L. Wang, *Phys. Rev. B* **63**, 125407 (2001).

37. S. Habenicht, K.P. Lieb, J. Koch, A.D. Wieck, *Phys. Rev. B* **65**, 115327 (2002).

38. W.L. Chan, N. Pavenayotin, E. Chason, *Phys. Rev. B* **69**, 245413 (2004).

39. S. Ichim, M.J. Aziz, *J. Vac. Sci. Technol., B* **23**, 1068 (2005).

40. T.M. Mayer, D.P. Adams, M.J. Vasile, K.M. Archuleta, *J. Vac. Sci. Technol., A* **23**, 1579 (2005).

41. J.L. Gray, S. Atha, R. Hull, J.A. Floro, *Nano Lett.* **4** (12), 2447 (2004).

42. M.J. Aziz, *Mat. Fys. Medd. Dan Vid Selsk* (2006) in press.

43. M.A. Makeev, R. Cuerno, A.L. Barabasi, *Nucl. Instrum. Methods Phys. Res., Sect. B* **197**, 185 (2002).

44. R. Levi-Setti, T.R. Fox, K. Lam, *Nucl. Instr. Meth.* **205**, 299 (1983).

45. B.W. Kempshall et al., *J. Vac. Sci. Technol., B* **19**, 729 (2001).

46. M. Castro, R. Cuerno, L. Vazquez, R. Gago, *Phys. Rev. Lett.* **94**, 016102 (2005).

47. H.H. Chen et al., *Science* **310**, 294 (2005).

48. J. Teichert, L. Bischoff, B. Kohler, *Appl. Phys. Lett.* **69** (11), 1544 (1996).

49. A. Cuenat, M.J. Aziz, in *Mater. Res. Soc. Symp. Proc.* **696**, E.A. Stach, E.H. Chason, R. Hull, S.D. Bader, Eds. (2002) pp. 31–36.

50. W.J. MoberlyChan, T.E. Felter, M.A. Wall, *Microsc. Today*, 28 (November 2006).

51. D. Santamore, K. Edinger, J. Orloff, J. Melngailis, *J. Vac. Sci. Technol., B* **15**, 2346 (1997).

52. A. Cuenat, *Adv. Mater.* **17**, 2845 (2005).

53. D.P. Adams, M.J. Vasile, T.M. Mayer, V.C. Hodges, *J. Vac. Sci. Technol., B* **21**, 2334 (2003).

54. U. Wendt, G. Nolze, H. Heyse, *Microsc. Microanal.* **12** (suppl. 2), 1302 (2006).

55. W.J. MoberlyChan, S. Reyntjens, A.M. Minor, *Microsc. Microanal.* **12** (suppl. 2), 1268 (2006).

56. U. Valbusa, C. Boragno, F. Buatier de Mongeot, *J. Phys.: Condens. Matter* **14**, 8153 (2002).

57. A.D. Brown, J. Erlebacher, W.L. Chan, E. Chason, *Phys. Rev. Lett.* **95**, 056101 (2005).

58. A. Stanishevsky, *Thin Solid Films* **398–399**, 560 (2001).

59. D.P. Adams, T.M. Mayer, M.J. Vasile, K. Archuleta, *Appl. Surf. Sci.* **252**, 2432 (2006).

60. P.E. Russell et al., *J. Vac. Sci. Technol., B* **16** (4), 2494 (1998).

61. G. Carter, *J. Appl. Phys.* **85** (1), 455 (1999).

62. A. Lugstein, B. Basnor, E. Bertagnolli, *J. Vac. Sci. Technol., B* **20**, 2238 (2002).

63. W.J. MoberlyChan, *Mater. Res. Soc. Symp. Proc.* **960**, N10-02 (2006).

64. D.P. Adams, M.J. Vasile, T.M. Mayer, *J. Vac. Sci. Technol., B* **24** (4), 1766 (2006).

65. T. Ishitani, T. Yaguchi, *Microsc. Res. Technol.* **35**, 320 (1996).

66. T. Ihsitani, T. Ohnishi, *J. Vac. Sci. Technol., A* **9**, 3084 (1991).

67. M.J. Vasile, J. Xie, R. Nassar, *J. Vac. Sci. Technol., B* **17** (6), 3085 (1999).

68. S. Facsko et al., *Phys. Rev. B* **69**, 153412 (2004).

69. M.A. Karolewski, *Nucl. Instrum. Methods Phys. Res., Sect. B* **230**, 402 (2005); Kalypso software, www.geocities.com/karolewski/Kalypso.

70. P. Tosin, A. Blatter, W. Luthy, *J. Appl. Phys.* **76** (6), 3797 (1995).

71. A.M. Ozhan et al., *Appl. Phys. Lett.* **75** (23), 3716 (1999).

72. E. Coyne, J. Magee, P. Mannion, G. O'Connor, *Proc. SPIE* **4876**, 487 (2003).

73. J.N. Brooks, *Fusion Eng. Des.* **60**, 515 (2002).

74. T. Ishitani, H. Koike, T. Yaguchi, T. Kamino, *J. Vac. Sci. Technol., B* **16** (4), 1907 (1998).

75. J.R. Michael, *Microsc. Microanal.* **12** (2), 1248 (2005).

76. G. Carter, *Vacuum* **80**, 475 (2006).

77. M. Kammler, R. Hull, M.C. Reuter, F.M. Ross, *Appl. Phys. Lett.* **82**, 1903 (2003).

78. A.A. Bergman et al., *Langmuir* **14**, 6785 (1998).

79. K. Gamo et al., *Jpn. J. Appl. Phys.* **23**, L293 (1984).

80. G.M. Shedd, H. Lezec, A.D. Dubner, J. Melngailis, *Appl. Phys. Lett.* **49**, 1584 (1986).

81. H.C. Kaufmann, W.B. Thompson, G.J. Dunn, *Proc. SPIE* **632**, 60 (1986).

82. L.R. Harriott, M.J. Vasile, *J. Vac. Sci. Technol., B* **6**, 1035 (1988).

83. R.L. Kubena, F.P. Stratton, T.M. Mayer, *J. Vac. Sci. Technol., B* **6**, 1865 (1988).

84. M.E. Gross, L.R. Harriott, R.L. Opila Jr., *J. Appl. Phys.* **68**, 4820 (1990).

85. P.G. Blauner, J.S. Ro, Y. Butt, J. Melngailis, *J. Vac. Sci. Technol., B* **7**, 609 (1989).

86. R.J. Young, J.R.A. Cleaver, H. Ahmed, *J. Vac. Sci. Technol., B* **11** (2), 234 (1993).

87. J. Funatsu, C.V. Thompson, J. Melngailis, J.N. Walpole, *J. Vac. Sci. Technol., B* **14**, 179(1996).

88. M.J. Vasile, L.R. Harriott, *J. Vac. Sci. Technol., B* **7**, 1954 (1989).

89. J.S. Ro, C.V. Thompson, J. Melngailis, *Thin Solid Films* **258**, 333 (1995).

90. T.P. Chiang, H.H. Sawin, C.V. Thompson, *J. Vac. Sci. Technol., A* **15**, 3104 (1997).

91. A.D. Dubner, A. Wagner, J. Melngailis, C.V. Thompson, *J. Appl. Phys.* **70**, 665 (1991).

92. J. Melngailis, *Proc. SPIE* **1465**, 36 (1991).

93. V. Ray, *J. Vac. Sci. Technol., B* **22** (6), 3008 (2004).

94. T. Ishitani, T. Ohnishi, Y. Kawanami, *Jpn. J. Appl. Phys.* **29**, 2283 (1990).

95. M.J. Vasile et al., *Rev. Sci. Instrum.* **62**, 2167 (1991).

96. See the article by M. Uchic et al. in this issue.

97. J. Melngailis, *J. Vac. Sci. Technol., B* **5**, 469 (1987).

98. L.R. Harriott, *Appl. Surf. Sci.* **36**, 432 (1989).

99. W.P. Economou, D.C. Shaver, B. Ward, *Proc. SPIE* **773**, 201 (1987).

100. M. Yamamoto et al., *Proc. SPIE* **632**, 97 (1986).

101. R. Puers, S. Reyntjens, D. De Bruyker, *Sens. Actuators, A* **97–98**, 208 (2002).

102. S. Khizroev, J.A. Bain, D. Litvinov, *Nanotechnology* **13**, 619 (2002).

103. E.M. Ford, H. Ahmed, *Appl. Phys. Lett.* **75**, 421 (1999).

104. T.W. Ebbesen et al., *Nature* **382**, 54 (1996).

105. A.J. Demarco, J. Melngailis, *J. Vac. Sci. Technol., B* **17**, 3154 (1999).

106. T. Morita et al., *J. Vac. Sci. Technol., B* **21**, 2737 (2003).

107. R. Kometani et al., *Microelectron. Eng.* **83**, 1642 (2006).

108. J.-F. Lin, J.P. Bird, L. Rotkina, P.A. Bennett, *Appl. Phys. Lett.* **82**, 802 (2003).

109. E.J. Sanchez, J.T. Krug, X.S. Xie, *Rev. Sci. Instrum.* **73** (11), 3901 (2002).

110. A. Botman, J.J.L. Mulders, R. Weemaes, S. Mentink, *Nanotechnology* **17**, 3779 (2006).

111. P.G. Blauner et al., *J. Vac. Sci. Technol., B* **7**, 1816 (1989).

112. A.N. Campbell et al., *Proc. 23rd Int. Symp. Testing Failure Analysis* (1997) p. 223.

113. K. Edinger, J. Melngailis, J. Orloff, *J. Vac. Sci. Technol., B* **16**, 3311 (1998).

114. S. Reyntjens, R. Puers, *J. Micromech. Microeng.* **10**, 181 (2000).

115. M. Ishida et al., *J. Vac. Sci. Technol., B* **21**, 2728 (2003).

116. K.-I. Nakamatsu et al., *J. Vac. Sci. Technol., B* **23**, 2801 (2005).

117. T. Tao, J. Ro, J. Melngailis, *J. Vac. Sci. Technol., B* **8**, 1826 (1990).

118. N. Smith et al., *J. Vac. Sci. Technol., B* **24** (6), 2902 (2006).

119. T.M. Mayer, S.D. Allen, *Thin Film Processes II*, J.L. Vossen, W. Kern, Eds. (Academic Press, New York, 1991) pp. 621–670.

120. FEI Co. SPI-mode technology, www.feico.com.

121. Zeiss technology, www.smt.zeiss.com/nts. □